Quantitative SPECT Imaging

18

Michael Ljungberg

Contents

18.1 Introduction

A scintillation camera is essentially a device that measures two-dimensional (2D) images of a radionuclide distribution in vivo by detecting emitted photons. Due to the construction of the collimator, events in the image obtained from photons emitted from different source depths will be superimposed, and the source depth will not be resolved. The solution is to obtain the three-dimensional (3D) information by measuring projections in different views around the patient and use a reconstruction algorithm. The method is called single-photon emission computed tomography (SPECT). If the activity is not redistributed between organs or tissues over the time of the measurement, then the assumption in any reconstruction method is that there exists an activity distribution for which a corresponding photon emission will result in the projections that are acquired by the system. The goal then, is to determine this distribution in 3D as accurately as possible.

18.2 Factors That Degrade SPECT Imaging

Presently, tomographic image reconstruction in SPECT is often based on iterative methods, such as the maximum likelihood expectation maximisation (ML-EM) and ordered subsets expectation maximisation (OS-EM) methods [1–3]. The approach is to find an activity distribution (described by a set of consecutive 2D tomographic images representing different sections in

M. Ljungberg (✉)
Department of Medical Radiation Physics,
Lund University, Lund, Sweden
e-mail: Michael.Ljungberg@med.lu.se

© Springer Nature Switzerland AG 2021
M. M. Khalil (ed.), *Basic Sciences of Nuclear Medicine*,
https://doi.org/10.1007/978-3-030-65245-6_18

the object) that produces the best match to the measured projection data. However, if the measured data suffers from physical effects, such as photon attenuation in the object or unwanted contribution to the projection data from photons scattered in the patient, then the reconstructed solution will not accurately describe the activity distribution. Photon attenuation can actually result in false positive indications, especially in non-homogeneous regions such as the thorax. It is, therefore, important to correct for these effects even if the actual numerical pixel values are of less importance.

The following examples that describe the major factors that degrade SPECT imaging have been created by the use of the Monte Carlo program SIMIND [4, 5] which simulated a cylindrical water phantom and the XCAT anthropomorphic mathematical phantom [6, 7]. The Monte Carlo method allows for the simulation of the photons from their emission from an object to the detection by a scintillation camera. During this process, it is possible to keep track of the interaction history of the photons and observe how the image is formed from these photons. The advantage of categorising each event in the image based on the origin of the photon i.e. primary, scattered, or penetrated photons, is that this makes it possible to study the degradation in detail. The relative activity concentration, defined for the XCAT simulations, were 90, 20, 90, 50, 30, 20 and 1 for the cardiac, the liver, both kidneys, the spleen, gall-bladder, bone and the background, respectively. A simulated perfusion defect with the size of about 10 cm^3 having a 25% uptake relative to the cardiac activity concentration of 90 were also defined.

Different photon energies have been simulated for visualisation, but some of these energies may not be clinically relevant to the simulated radionuclide distribution. A standard Anger-type camera has been simulated with a 3/8-in. crystal thickness and an energy resolution of 9.0% FWHM at 140 keV. Projections were scaled to represent 300 MBq in the XCAT phantom and 30 s acquisition time to define a clinical realistic noise level when applied. Reconstruction were made using an in-house developed filtered back projection algorithm and the IRL iterative reconstruction software, developed by Frey and Tsui at the Johns Hopkins Medical Center, Baltimore, USA. Included in this package are the ESSE model-based scatter correction [8] and compensation for collimator resolution.

18.2.1 Distance-Dependent Collimator Resolution

The commonly used parallel-hole collimator has the advantage of having a geometrical sensitivity that is independent of the source-to-collimator distance within the field of view (FOV). This means that the conversion factor (cps/MBq) remains constant within the FOV, which greatly simplifies the process of activity quantitation. The spatial resolution, however, depends on the distance to the collimator and the specifications of the holes (diameter, shape, septum thickness and length). In a clinical environment, it is common to have several types of collimators available, which are selected depending on the type of study and energy of the photon. Examples are low-energy high-resolution (LEHR), low-energy general-purpose (LEGP), medium-energy (ME) and high-energy (HE) collimators. Because of the underlying design, even a parallel-hole LEHR collimator will limit the spatial resolution to a best possible value of approximately 10–15 mm for SPECT. This means that although the correct number of counts are acquired by the camera, the position of each event is spread out over a large area (more pixels) if the source is located at a larger distance. This effect can be observed in Fig. 18.1 where profiles through images of three-point sources being located at different distances from the collimator surface are shown for LEGP, LEHR, ME and HE collimators. The profiles show a larger value of the FWHM as the source moves away from the camera. This broadening is less pronounced for the LEHR collimator, but at the expense of a reduction in the measured count rate.

The distance-dependent blurring of an image means that the cps/pixel will not reflect the MBq/ml in a particular voxel. This unwanted effect is called the partial volume effect. The spatial resolution also affects the image contrast and hence the ability to detect small lesions of moderate and low

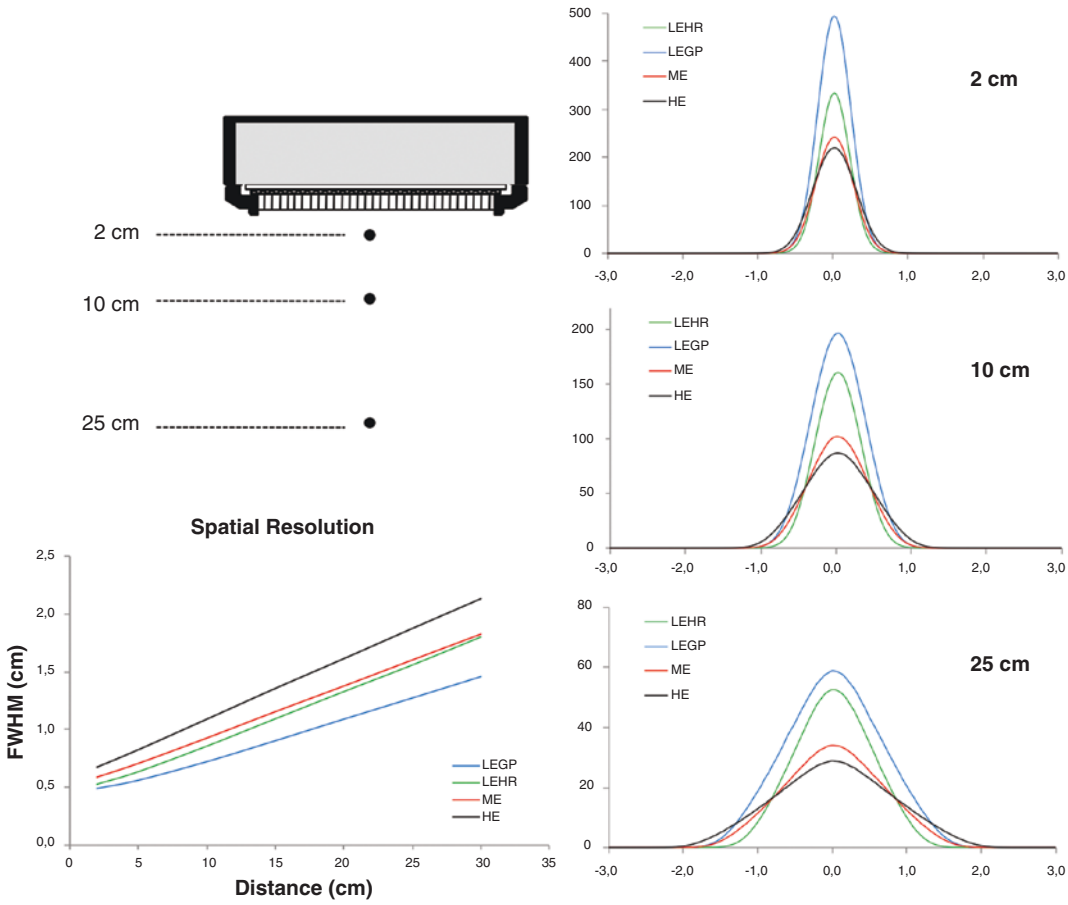

Fig. 18.1 Simulated point-spread function for a ^{99m}Tc point source (140 keV) located at distances of 2, 10 and 25 cm to the lower collimator surface. The images illustrate the importance of always keeping the camera as close as possible to the patient surface. The figure also shows that the magnitude of the degradation in spatial resolution for the four collimators also differs. The activity was the same for all locations and collimators

lesion-to-background activity ratios. In principle, very small lesions can be detected, but the lesion-to-background activity ratios in these cases needs to be very high; however, the smallest volume of a lesion that can be measured should be equal to the order of the spatial resolution of the system.

18.2.2 Photon Attenuation

Some of the photons emitted from the radiopharmaceutical administered to a patient will interact within the patient and therefore not contribute to image formation in the expected way, as can be seen in Fig. 18.2. The basic interaction types for photon energies that are important for nuclear medicine applications are photoabsorption, Compton interaction (photon scattering with energy loss), coherent interaction (photon scattering without energy loss) and pair production (rare since this interaction type can only occur for photons with energies above 1.022 MeV). Consider a rate of photons impinging in a narrow-beam geometry on an object of the thickness d and the density ρ. The number of photons that pass through the object is given by

$$\dot{N} = \dot{N}_0 \cdot e^{-\frac{\mu}{\rho} \cdot \rho \cdot d} \tag{18.1}$$

where $\dot{N}_0$ is the initial narrow-beam photon rate and $\dot{N}$ is the photon rate after passing though the object. The probability of each of the possible interactions can be described by differential cross-section coefficients, and, consequently, the

sum of these coefficients describes the probability of occurrence of any type of interaction. This sum of the coefficients is proportional to the *linear* attenuation coefficient μ.

$$\mu \sim \tau_{\text{photo}} + \sigma_{\text{compton}} + \sigma_{\text{rayleigh}} + \kappa_{\text{pair}} \quad (18.2)$$

Photon attenuation depends on the photon energy ($h\nu$), atomic numbers of the composition (Z) and the density (ρ), and values are often tabulated as *mass*-attenuation coefficients, μ/ρ.

In a photo absorption event, the energy of a photon is transferred to an electron in the interacting atom. This electron will, if the photon energy is high enough, liberate itself from the atom and leave the atom with a kinetic energy equal to the incoming photon energy minus the binding energy of the electron. When the vacancy in the electron shell is filled with an outer electron, the binding energy is emitted either as a characteristic X-ray photon or as an Auger electron. The probability for these occurrences depends on the atomic number of the material. Auger electron emission is dominant in low-Z tissue-equivalent materials (Fig. 18.3).

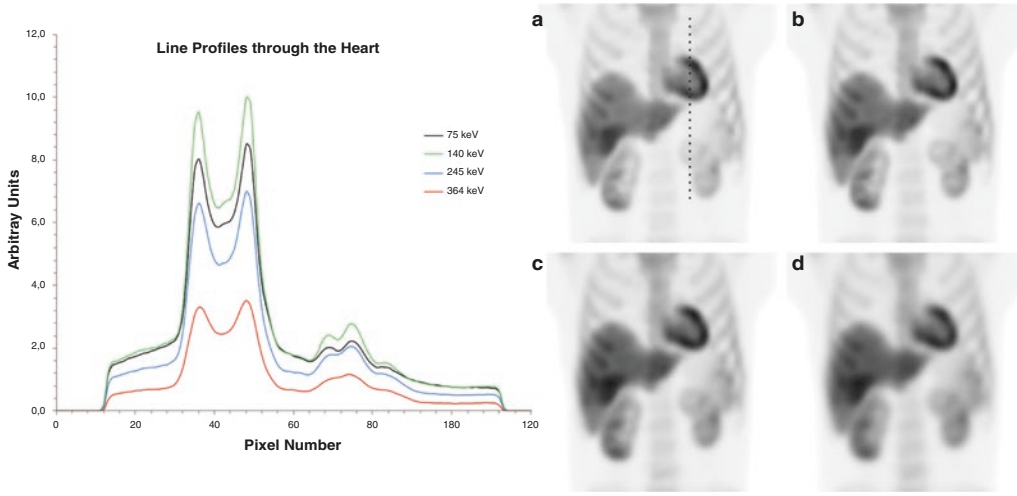

Fig. 18.2 Four frontal projections of the XCAT phantom showing the effect of photon attenuation in the cases of 75 keV (**a**), 140 keV (**b**), 208 keV (**c**) and 364 keV (**d**) photon emission, respectively. Vertical line profiles through the heart and part of the left kidney have been calculated and are compared in the left diagram. The dotted line in projection (**a**) indicates the location of the profiles. Note that these figures were simulated considering photon attenuation alone. For a complete ^{131}I decay, additional counts are added generated by high-energy photons—637 keV (7.12%) and 723 keV (1.78%)—and backscattered from the compartment behind the crystal and by septal penetration

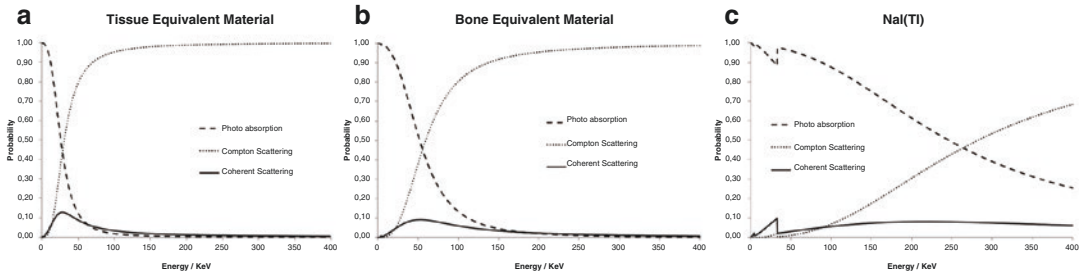

Fig. 18.3 Relative probability for photo-absorptions, Compton scattering and coherent scattering in the energy range up to 400 keV for (**a**) tissue-equivalent material, (**b**) bone-equivalent material and (**c**) NaI(Tl) crystal material. Note the rapid decrease in probability for photo absorption in tissue. Note also that these data are relative, and that the magnitude of the attenuation is much larger for NaI(Tl) as compared to water

18.2.3 Photon Scattering

Photon scatter originates from the limitation of the scintillation camera to accurately measure the energy imparted to the NaI(Tl) crystal. The processes of converting the imparted energy to visible light photons and guiding these photons to the photomultipliers to achieve measurable signals are inherently stochastic. Therefore, the measured signal will have a statistical error even if the imparted energy always remains the same. For new NaI(Tl) crystals, this statistical error is approximately 8–10% (FWHM) for an absorbed energy of 140 keV. This relatively large error implies that an energy discriminator needs to cover about twice this width (16–20%) in order to maintain a reasonable counting statistic. Some of the photons that have been scattered in the patient with a small deflection angle (small loss of energy) may therefore be detected within such a large energy window and thus contribute to the image formation; however, these photons carry wrong spatial information about the location of decay in the object. Such scattered events will result in a degraded image contrast and present a potential problem when trying to quantify regional activity uptakes.

Figure 18.4 shows the true imparted energy in the NaI(Tl) crystal from 140 keV photons (^{99m}Tc), emitted from a point source in centre of a 11 cm radius cylindrical water phantom (18.4a). Note the sharp peak that occurs because the full-absorption from 140 keV photons will be within the same energy channel. Plot 18.4b shows simulated data corresponding to a measured energy spectrum. The peaks are broader due to the poor energy resolution of the camera (9% FWHM at 140 keV). Because of this inaccuracy in the energy measurement, some photons that have been scattered in the phantom are detected within the energy window. Plot 18.4b

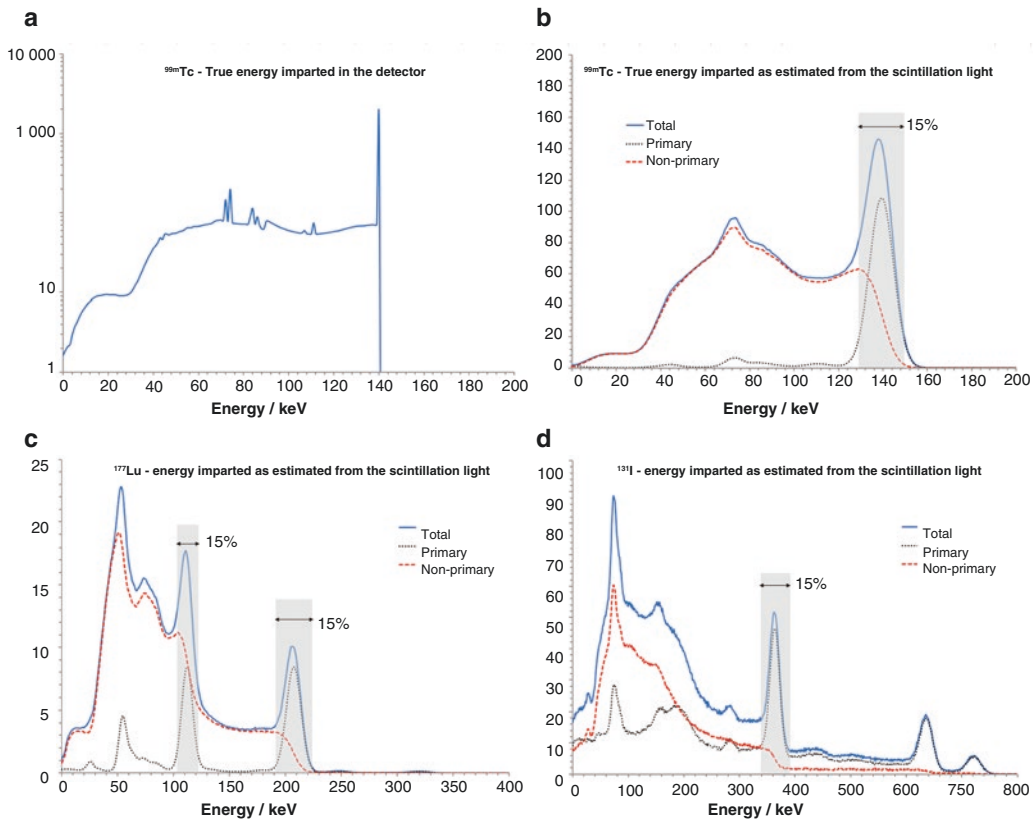

Fig. 18.4 Plot (**a**) shows the true imparted energy in the NaI(Tl) crystal from 140 keV photons (^{99m}Tc) emitted from a point source in centre of a 11 cm diameter cylindrical water phantom. Plot (**b**) displays curves that represent events from primary unattenuated photons and photons scattered in the object. Plots (**c**) and (**d**) show corresponding data for ^{177}Lu and ^{131}I

also displays curves that represent events from primary unattenuated photons and photons scattered in the object. Note that a substantial fraction of scattered photons will contaminate the images acquired within the energy window. In the acquired image, it is not possible to distinguish these events from the primary events. Plots 18.4c and d show corresponding data for ^{177}Lu and ^{131}I.

The energy $h\nu'$ of a scattered photon is directly related to the angle of deflection according to the Compton equation

$$h\nu' = \frac{h\nu}{1+\frac{h\nu}{m_o c^2}\left(1-\cos\theta\right)} \tag{18.3}$$

For higher photon energies, the scattering angles θ tend to peak in the forward direction, but at moderate photon energies (~100 keV) the distribution is relatively symmetrical with a slightly lower probability for scattering angles ±90°. The differential cross-section, as described by the Klein-Nishina relation is given as

$$d\sigma^{e}_{\gamma,\gamma e} = \frac{r_e^2}{2}\cdot\left(\frac{h\nu'}{h\nu}\right)^2\cdot\left(\frac{h\nu}{h\nu'}+\frac{h\nu'}{h\nu}-\sin^2\theta\right)\cdot \mathrm{d}\Omega \tag{18.4}$$

which determines the probability for a photon being scattered through an angle θ into a solid angle dΩ relative to the incoming photon trajectory. Eq. (18.4) has been derived based on the assumption that the electron is not bound to the nucleus and in rest. When the photon energy decreases, the binding effect to the nucleus changes the cross-sections slightly.

Since the contribution of scatter in a SPECT projection is a consequence of photon interactions in the object, the amount of scatter (sometimes defined as the scatter-to-total fraction) depends on photon energy, source depth and distribution, and tissue composition in addition to camera-related parameters such as energy resolution and energy window settings. Figure 18.5 shows the variation of the scatter-to-total fraction with these parameters and brings out the different dependences.

From Fig. 18.5a, it can be seen that the scatter-to-total fraction increases with increasing source depth but levels out at or above a moderate source depth (>20 cm). This is because, although the scattering increases with depth, the scattered photons will also be more attenuated compared to the primary photons with higher energies. The degradation in image quality due to Compton scattering is also a function of the energy resolution and thus, the related energy window setting; however, as can be seen from Fig. 18.5b and c, the dependence of these two parameters is quite moderate. Thus, even for new crystals, the scatter-to-total fraction in a scintillation camera image remains quite high (30–50%).

When reviewing tabulated cross-sections for Compton scattering [9], one can see that the relative number of Compton scattering interactions increases with increasing photon energy, as can be seen in Fig. 18.2. It is, therefore, somewhat contradictory that issue of scatter in SPECT is more considerable for photons of low energies (Fig. 18.4d). This happens because a fixed energy window centred on the photo-peak energy is used here. For an initial high photon energy, the relative loss of energy to a secondary electron during a Compton scattering is quite large, which results in a scattered photon of significantly lower energy when compared to using the energy window discriminator in the lower part of the energy distribution. For a lower initial photon energy, the relative loss of energy in a Compton scattering is small, which implies that even for a large scattering angle there is a good chance that a scattered photon in that energy range will be detected within the fixed energy window.

18.2.4 Collimator Septal Penetration

As mentioned above, the purpose of the collimator is to select only those photons emitted in a direction determined by the axial direction of the collimator hole and to reject all other photons. However, because of the exponential characteristics of photon attenuation, there will always be a finite probability for a photon to penetrate the collimator walls (septa) and interact in the crystal

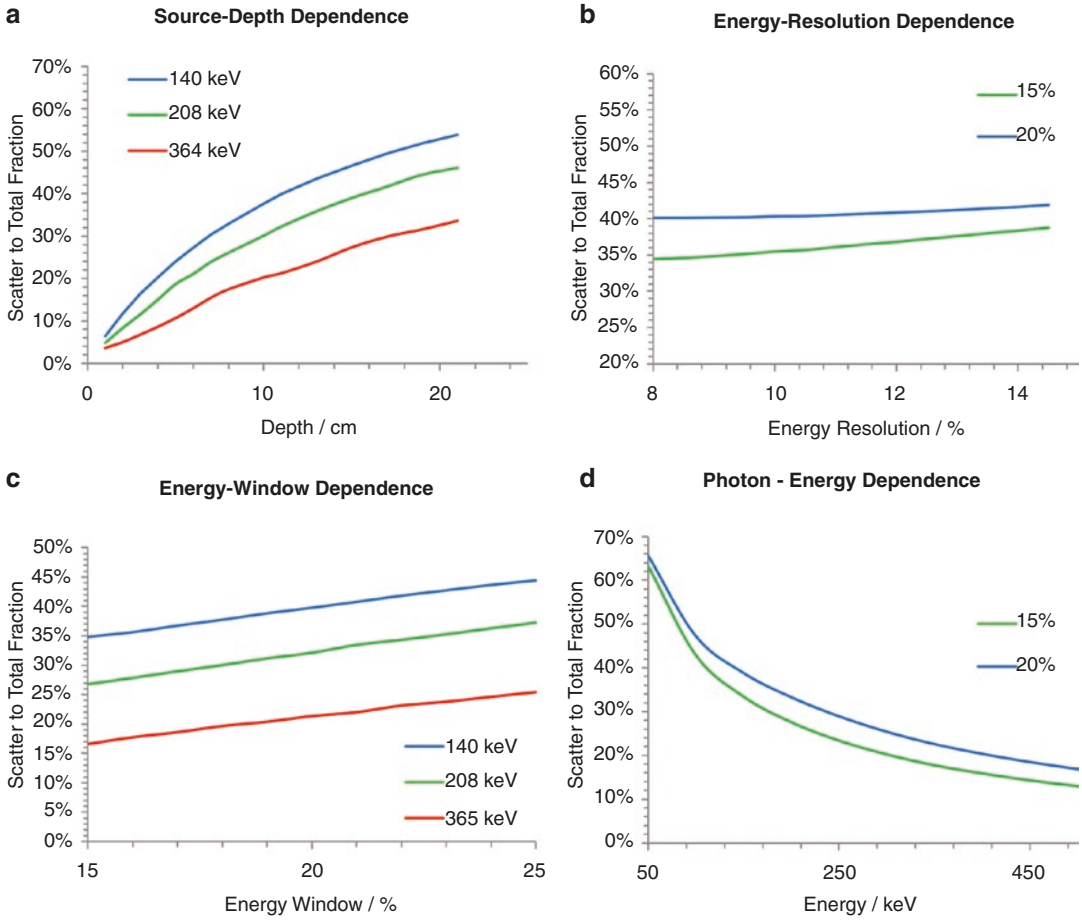

Fig. 18.5 Scatter-to-total dependence on (**a**) source depth, (**b**) energy resolution of the camera, (**c**) energy window setting and (**d**) photon energy. Two energy windows of 15% and 20% have been used when appropriate. The data have been simulated using a cylindrical water phantom of 15 cm radius and 20 cm length. The point source is located at the centre of the phantom for the results in graph (**b**)–(**d**)

further away from the positions defined by the location of the hole. When constructing a collimator, the selection of wall thickness is, therefore, a compromise among the spatial resolution, system sensitivity and probability of septum penetration.

To illustrate this effect, consider the simulated images shown in Fig. 18.6. The upper row shows three images of a simulation with ^{99m}Tc photons and for LEHR, ME and HE collimator—it can be observed that the image has good quality although the HE collimator provide less spatial resolution. The second row of images shows a simulation with photons of ^{177}Lu for the same set of collimators. Here we see a clear influence of septal penetration for the LEHR collimator, but the other two collimators have sufficient collimator septa thicknesses to minimise the contribution of penetration. The third lower row shows the same simulation for a complete ^{131}I decay. The image for the LEGP collimator is completely deteriorated due to septum penetration and is unusable. Because of the thicker septa of the HE the penetration effects have been reduced and satisfactory image quality has been obtained. Penetration effect can also be seen for the ME collimator. Even when using a HE collimator, penetration will occur since the complete decay of ^{131}I also include the higher photon energies of

637 keV (7.3%) and 723 keV (1.78%). Even though the number of emission per decay of these photons may be low, the high photon energies enables them to penetrate the walls even when an HE collimator is used [10] and these significantly interfere with the image formation.

The unfavourable effects of septum penetration can be reduced either by using a collimator with thicker septa [11] and better attenuating properties, such as tungsten, or the by accounting for the phenomenon using a suitable correction method. If the septum penetration can be modelled, then this effect can be included as a collimator-response function in the forward projection step in an iterative reconstruction method.

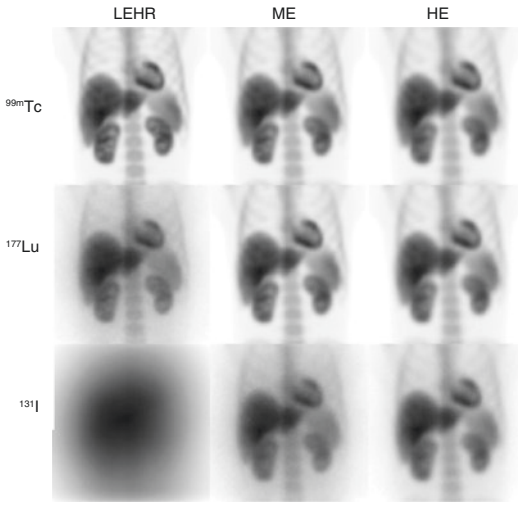

Fig. 18.6 The upper row show images photons of ^{99m}Tc impinging on a camera with LEHR, ME and HE collimators. The middle row and lower row show the same simulation but for photons of ^{177}Lu and ^{131}I, respectively. The images are noise-free for a better visualisation of the effects

To summarise some of these effects, consider the energy spectra displayed in Figs. 18.4b–d and the results in Table 18.1 obtained from these simulations. It can be seen from Table 18.1 that for ^{99m}Tc, there is a significant fraction of non-primary events, mainly due to photon scattering in the object. The penetration fraction is very small, which indicates that the collimator is effective in absorbing photons moving in unwanted directions. For the 208-keV peak energy window of ^{177}Lu, the incidence of non-primary and penetration events is also relatively moderate when using the ME collimator a s compared to, but the fraction of penetration is somewhat larger than for ^{99m}Tc, possibly due to the 321 keV photons in the decay scheme that, despite the low abundance of 0.22%, may contribute to these events due to the increased probability for septal penetration. For the 113 keV peak energy, however, the penetration fraction is low, but the non-primary fraction is very high. This is due to single- and multiple- Compton scatterings of the 208 keV photon which results in photon absorptions detectable in the 113 keV peak energy window.

When using the LEHR collimator for ^{177}Lu imaging, the data in Table 18.1 show that the non-primary fraction is relatively large, and that there is a large fraction of penetration for the 208 keV photons. The cps/MBq is higher, but this results from unwanted counts and hence, does not justify the use of an LEHR collimator. For the simulation of ^{131}I, one can see that the fraction of non-primary events are large mainly due to the

Table 18.1 Count rate per unit activity (cps/MBq) is shown together with the fraction non-primary/total and penetrations/total for three different radionuclides

Radionuclide	Peak energy (keV)	cps/MBq		Non-primary/total		Penetration/total	
		15% window	20% window	15% window	20% window	15% window	20% window
^{99m}Tc (LEHR)	140 (89.1%)	21.5	24.6	39.3%	44.8%	3.2%	3.2%
^{177}Lu (ME)	208 (10.38%)	1.9	2.1	34.0%	39.2%	5.0%	4.9%
	113 (6.2%)	2.6	3.0	65.6%	69.2%	1.3%	1.3%
^{177}Lu (LEHR)	208 (10.38%)	5.2	5.6	76.0%	77.6%	44.2%	43.2%
	113 (6.2%)	2.9	3.5	70.3%	73.7%	10.1%	10.8%
^{131}I (HE)	364 (81.2%)	15.2	17.4	60.2%	64.9%	23.6%	23.5%

large contribution from the penetration of the 636 and 723 keV photons and also the potential contribution from these photons when they backscatter from the material surrounding the NaI(Tl) crystal.

18.2.5 Physiologic and Patient Motions

When acquiring data with a SPECT camera, one should always remember that the acquisition is made using a 'camera shutter' that is open during the entire acquisition time. This means that movement of the patient will result in a degradation of the spatial resolution and in some cases, cause artefacts. Even if the patient is carefully strapped and remains very still, some movements such as respiratory movements and motion of the heart cannot be avoided [12].

Respiratory movements cause spatial changes that depend on the organ. Since the frequency of the breathing is different from the frequency of cardiac motion, respiratory movements will also have an effect on the quality of cardiac imaging even if the gated SPECT is applied. The motion is complicated with translations in the axial or superior/inferior direction causing a blurred image with a potential reduction of counts in the anterior and inferior walls. In tumour detection, the form of the tumour may change to a more elongated or elliptical shape because of breathing and the results may also have a lower image contrast. This has been observed in lung studies with PET and ^{18}FDG.

18.2.6 Image Noise

Because of the randomness of photon histories, an acquired SPECT image will be affected by statistical errors and related image noise. The noise distribution of the scintillation camera image follows the Poisson distribution where the variance of a measure in a region of interest is the sum of the counts. This implies that in order to get a good image quality, a sufficiently long acquisition time together with a high administered activity should be used. Noise in the image also depends on the selected matrix size. Changing from the matrix size of 64 × 64 to 128 × 128 will increase the variance in a projection pixel by a factor of four. Note also that reconstruction is usually performed slice by slice, which means that the slice thickness (and consequently the acquired number of counts) is half for a 128 × 128 matrix as compared to a 64 × 64 matrix. The mean counts per voxel in a reconstructed SPECT image will, therefore, be reduced by a factor of eight. Thus, it is not always advantageous to increase the matrix size. The time per projection and the number of projections is also of importance. These factors need to be optimised for each study since noise due to improper acquisition parameters can propagate through the reconstruction process and create artefacts in the final image.

18.2.7 Other SPECT Degradation Factors

It is essential that the scintillation camera is well tuned and calibrated. This is especially true for SPECT since deficiencies can result in visible artefacts. For example, non-uniformities in a planar image can be of less importance and sometimes difficult to detect, but when reconstructing data from a SPECT camera with non-uniform regions, artefacts can be seen as distinct rings in the image. The tuning of the centre-of-rotation (COR), that is, the alignment of the electronic centre used in the reconstruction algorithm to the mechanical centre of the camera orbit is also important. A small error in the COR results in the degradation of spatial resolution, and if a larger shift occurs, then also here, a ring artefact may appear. It is also important to calibrate the pixel size carefully when performing the correction for attenuation as well as other quantitative measures. A wrong value can result in either under- or overcorrection due to errors in the parameter x in Eq. (18.1). Other factors that can influence the accuracy in a SPECT study are the selection of acquisition parameters and the related noise. The most important selection here is the number of

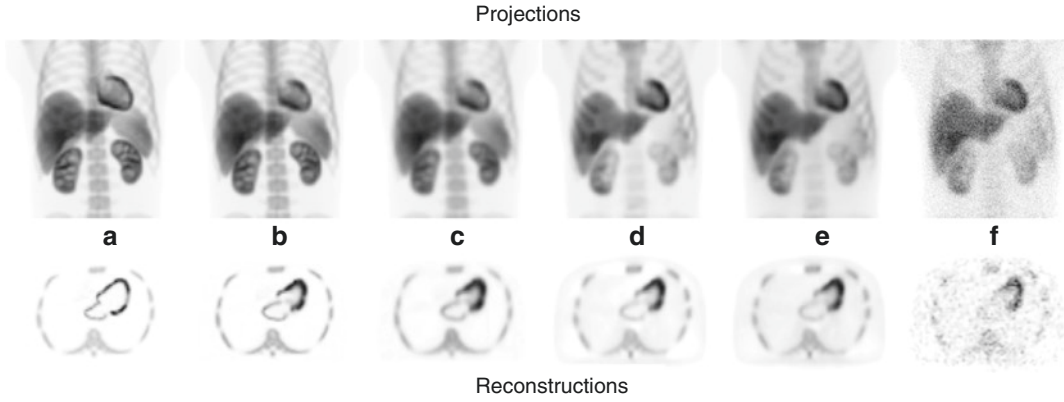

Fig. 18.7 Column (**a**) corresponds to an imaging situation without patient motion and a perfect camera resolution. Column (**b**) includes patient movements (respiration and heart beating). Column (**c**) represents an image with a typical system resolution and patient movements. Column (**d**) also includes photon attenuation. Column (**e**) includes photon attenuation and scatter contribution and column (**f**) is the same as column (**e**) but with noise added

projections and the matrix size. There is a relation between the expected spatial resolution in an image and the number of samples (angles and pixels) as determined by the Nyquist frequency and the number of angular intervals.

Reaching this frequency limit may, in some cases, be difficult depending on the activity administered to the patient and the time required for the acquisition. Generally, there is a trade-off among image quality (the combination of spatial resolution, image contrast and noise level), realistic acquisition times and levels of administered activity. Often, image processing including low-pass filtering are required, although it must be noted that post-acquisition image filtering requires a certain compromise of the spatial resolution. In some investigations where high administered activities are used, limitations in the count rate performance of the camera can result in unexpected results. Dead time problems and pulse pile-up effects can change the system sensitivity (cps/MBq) and calibration factors for scatter correction methods. In addition, significant mispositioning of events due to the unwanted contribution of scintillation light from earlier events may occur because the position of an event is calculated from the centroid of the emitted scintillation light. In this context, it should be remembered that calibrations made for low count rates might thus not be relevant in high count rate imaging.

As data is collected over a relatively long duration, it is important that the patient remains in the same position. Some movements such as cardiac motion and breathing are unavoidable. Cardiac motion can be accounted for using gated SPECT in which the cardiac cycle is divided into a number of separate time-frame acquisitions based on ECG information, especially the R-R interval. It has been standard practice for many years to collect information by this technique and display separately reconstructed images of the different time intervals in a cine-mode display. However, the image quality is most hampered due to noise because of the limited amount of the collected count for 8- or 16-frame gated SPECT. Spatial and temporal filtering is a pre-requisite here for a reasonable image quality. In addition, the number of projections and the number of time frames per cardiac cycle are often reduced in order to increase the time per projection for a given total acquisition time.

Figure 18.7 summarises how the image is degraded by the different factors discussed above. The upper row shows the frontal projections and the lower shows the corresponding reconstructed transversal images selected at a

certain location in the heart. Reconstructions were made with an iterative OS-EM algorithm without any corrections. The simulation was performed using 120-angle projections and a 360° rotation mode. The matrix size was 128 × 128, and eight iterations and ten subsets were used in the reconstruction. No post-filtering was applied to the reconstructed images. The first set of images (a) represents acquisition with a perfect system in the absence of cardiac or respiratory motion. The reconstructed image still shows some degradation in spatial resolution due to the finite sampling in projection angles, matrix size, and forward projection algorithm. The second column (b) shows the blurring due to respiratory and cardiac motion. When determining the attainable image quality in clinical studies based on phantom experiments, it is important to consider this motion since physical phantoms are most often static. In addition, the third column (c) includes the degradation in spatial resolution caused by the characteristics of the LEHR collimator. The fourth column (d) includes the attenuation of primary photons but no scatter contribution. This mimics a system with perfect energy resolution and a corresponding narrow energy window. The fifth column (e) includes the presence of scatter due to the limited energy resolution. The last column (f) shows the same images as in column (e) but with an added realistic noise level.

18.3 Correction Algorithms

The objective of a reconstruction method is to obtain a source distribution, described as a transversal image that matches the measured projections as accurately as possible. However, if the measured data are affected by photon attenuation, scatter and collimator blurring, the reconstructed images will not be accurate. It is, therefore, important that these physical effects need to be compensated for even if the numerical values in the final image are not very important, in order to obtain a high-quality diagnostic image with better sensitivity and specificity.

18.3.1 Attenuation Correction Methods

When using the filtered back projection method (FBP) to reconstruct images, an attenuation correction need to be applied either prior to or post the reconstruction step. As a pre-processing method, the conjugate-view method can be applied if opposite projection data are available. The main advantage is that the source depth dependence x in Eq. (18.1) becomes cancelled out when the opposite projections are combined by a geometrical-mean operator on a pixel-by-pixel basis. Let P_{ant} and P_{post} be the counts in opposite projections and P_{air} be the counts registered in both cameras without attenuation (assuming a parallel-hole collimator with invariant system sensitivity within the FOV). Then, the geometrical-mean is calculated using

$$\begin{aligned}\sqrt{P_{\text{ant}} \cdot P_{\text{post}}} &= \sqrt{\left[P_{\text{air}} \cdot e^{-\mu \cdot d}\right] \cdot \left[P_{\text{air}} \cdot e^{-\mu \cdot (T-d)}\right]} \\ &= \sqrt{P_{\text{air}}^2 \cdot e^{-\mu \cdot T}} \;=\; P_{\text{air}} \cdot e^{-\mu \cdot T/2}\end{aligned} \tag{18.5}$$

where d is the distance from the source to the surface along the projection line toward the anterior detector and T is the total thickness of the patient's body along the same projection line. The equation is only valid for point-like sources and uniform attenuation. Still, this method is used frequently in planar imaging activity quantitation.

The Chang method [13] is a postprocessing method that is applied to reconstructed SPECT images. The base for this method is the calculation of an attenuation factor averaged for all angles and determined for each voxel location within the boundary of the object. The method can be mathematically described as

$$\text{CF}(x,y) = \left[\frac{1}{N}\sum_{I=0}^{N} e^{-\mu \cdot d(x,y,\theta_i)}\right]^{-1} \tag{18.6}$$

If the information about heterogeneous attenuation, expressed as a map of varying μ values, can be obtained by some type of transmission study (see more about this below), then this informa-

tion can be included in the calculation of the attenuation factor. The method may result in imperfect attenuation compensation and has inferior noise properties.

Today, the most frequently used compensation method for attenuation forms part of an iterative reconstruction method. A common feature of all iterative reconstruction methods is the use of a calculated projection, obtained by forward projecting a first estimate of the activity distribution for the purpose of mimicking the image process. By comparing these calculated projections to match the measured projections using some kind of cost-function, the need for an improvement (often denoted 'an update') of the initial estimated activity distribution can be determined. Photon attenuation can be implemented both in the forward projection step before calculating the final projection bin and in the back projection step. Information about the non-uniform attenuation distribution can be included in the projection steps if appropriate attenuation maps are available either from transmission scans or registered CT images.

18.3.2 Measurement of Photon Attenuation

Properly correcting for attenuation in the thorax region requires a measurement of the distribution of attenuating tissue (an attenuation map) from a transmission measurement using an external radiation source mounted on the opposite side of the patient. For each SPECT projection angle, two measurements are required; one with the patient in situ and another blank study. By calculated the ratio between the two projections on a pixel-by-pixel basis, (j,j), line integrals (projections) of the attenuation coefficients can be calculated from the following formula

$$\int \mu_{h\upsilon_{em}}(i,j) = \mathrm{f}\left(h\upsilon_{tr}, h\upsilon_{em}\right) \cdot \left[-\ln\left(\frac{P(i,j)_{patient}}{P(i,j)_{blank}} \right) \right] \tag{18.7}$$

The function $f(h\upsilon_{tr}, h\upsilon_{em})$ includes normalisation factors and conversion of the μ values from the photon energy $h\upsilon_{tr}$ (or X-ray spectrum), used for the transmission study to the photon energy $h\upsilon_{em}$ used for the emission study. If the P projections have been obtained from a CT scan, then function f also needs to include a conversion from HU units to a relevant unit (e.g. using a HU-to-mass-density calibration). The actual method for the conversion to linear μ values is vendor-specific. The final μ-projections can then be reconstructed using either FBP or by iterative reconstruction methods.

If a radionuclide is used as a radiation source, it is generally desirable to have properties such that the transmission scan and emission scan can be done simultaneously. This implies that the radionuclide needs to be different from the main radionuclide in order to separate transmission data and have high activity. In earlier days, the most commonly used radionuclide in commercial systems was ^{153}Gd with a half-life of 242 days and the emission of two major photon energies of 97.5 keV (29.5%) and 103 keV (21.1%), respectively. The method with a radionuclide source suffers from several limitations. First, photons emitted from the main radionuclide (often ^{99m}Tc) that are scattered in the patient were registered in a lower transmission energy window. This led to too-low numerical values of the attenuation coefficients. Second, the source needed to be replaced on an approximately annual basis making the method relatively expensive. Third, the spatial resolution of the camera only resolved the major structures, such as the lungs, and so, the attenuation map could not be used as an anatomical reference map (Fig. 18.8).

The recent developments in combined SPECT/CT systems cancelled out most of the serious issues with radionuclide-based transmission measurements. The resolution and noise characteristics of modern systems are superior and consequently, the quality of the measured attenuation coefficients is, therefore, high. The scaling to other photon energies is relatively accurate despite the fact that the CT images are created from a broad spectrum of bremsstrahlung photon energies. The latest SPECT/CT models include diagnostic CT (spiral) with rapid scanning time and a spatial resolution that meets the requirement for a useful radiological diagnostic modal-

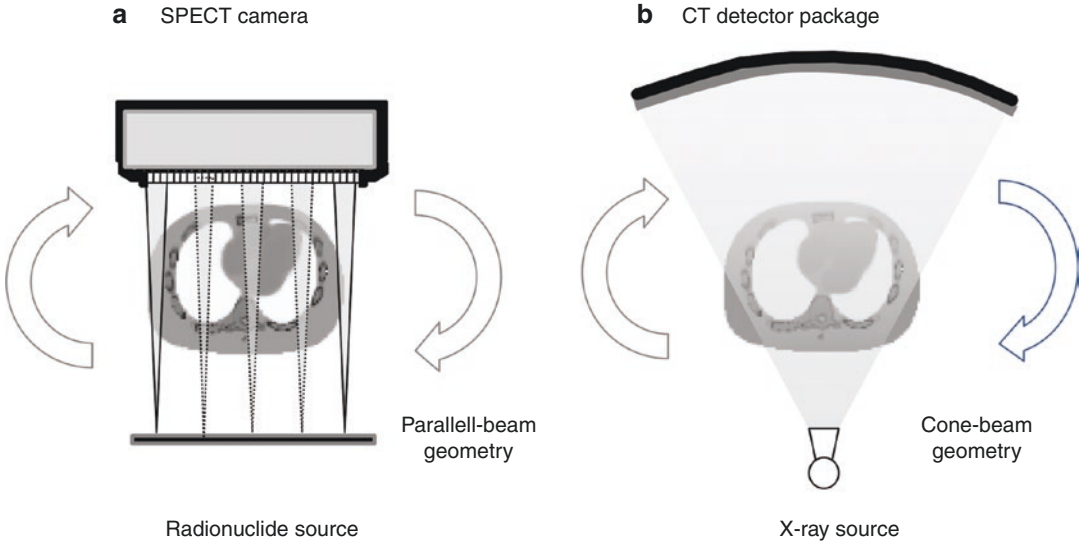

Fig. 18.8 Schematic image of detector principles behind transmission imaging. The the left (**a**), the transmission source was a radionuclide with a proper characteristic and placed on the gantry of the SPECT camera. The the right (**b**), a schematic figure shows the same principles for the CT, but where a ray tube with a cone-beam emission is used. The detector package is also different. In both cases, one also acquires a blank scan without the patient in site

ity in contrast to the first-generation SPECT/CT system that had a spatial resolution of approximately 34 mm. However, it must be noted that CT snapshots do not generally represent the average attenuation caused by the breathing that is 'seen' by the SPECT camera. Artefacts can, therefore, be introduced in an attenuation correction. For more information on the combined SPECT/CT system, see Chap. 14 in this textbook.

18.3.3 Scatter Correction Methods

Correction for scatter is most often made either in the energy domain where scatter in the photo-peak energy window is modelled by collected data in additional energy windows or by using analytical methods that model the scatter directly on photo-peak data directly. One of the early scatter corrections put forth was the dual-energy window method (DEW) proposed by Jaszczak et al. [14]. This method is based on an additional acquisition in a wide lower energy window. Scatter subtraction was applied by assuming that the distribution of counts in this lower energy window is qualitatively equal to the distribution of scatter in the photo-peak window, but only differ quantitatively by a scaling factor k (often set to 0.5 if the width of the scatter window and the main photo-peak window is the same). A scatter-corrected projection is then calculated from

$$P_{\text{primary}} = P_{\text{peak}} - k \cdot P_{\text{2nd}} \tag{18.8}$$

The main problem with this method is to obtain a proper value of k since this factor essentially is a function of the patient geometry and source distribution. Furthermore, the distribution of scatter in the lower energy window include a larger fraction of events created from multiple-scattered photons with wide angles, which may then cause either over- or under-corrections in specific regions even if the k factor is accurate.

A similar approach is used in the Triple-Energy Window (TEW) method, but this method is based on two narrow adjacently located energy windows around the photo-peak window [15]. By considering the average of the acquired images pixel-by-pixel and scaling by the ratio between the energy window width of the photo-peak window and the scatter windows, a better

scatter estimate will be obtained. A scatter-corrected projection is obtained from

$$P_{\text{primary}} = P_{\text{peak}} - \left[\frac{P_{\text{lower}}}{\Delta E_{\text{lower}}} + \frac{P_{\text{upper}}}{\Delta E_{\text{upper}}} \right] \cdot \frac{\Delta E_{\text{Peak}}}{2} \tag{18.9}$$

This method does not rely on any scaling factor. However, the main problem here is the noise in the scatter data that mainly results from the narrow energy windows, and scatter images require further processing such as low-pass filtering before subtraction. Nevertheless, this method has been successful not only for ^{99m}Tc studies but also for ^{131}I studies where the upper scatter window takes into account the down-scatter from the 637 and 723 keV photons which are emitted in the ^{131}I decay (Fig. 18.9).

Figure 18.10 shows simulated point-spread functions for different point source locations in an 11-cm radius cylindrical water phantom. The unscattered primary component has been separated and is shown as dashed lines. The shape of the scatter component in a point-spread function depends on the source depth to a large extent. For shallow source depths, the probability of multiple scattering is low, and therefore, the shape of the scatter profile is quite narrow. For a large source depth, the distribution becomes wider because of more events from multiple-scattered photons that results in registering a position far away from the decay location.

Frey and Tsui [16] has developed the effective scatter source estimator (ESSE) method, in which the modelling of the scatter is incorporated in an iterative reconstruction method using pre-calculated scatter functions. The method has been proven to be useful for several radionuclides and also efficient in calculating the crosstalk of scatter between two energy windows [17]. However, the method has only limited accuracy in non-homogeneous regions and in cases where an out-of-field-view of the activity becomes important.

The most advanced and potentially accurate methods available today are based on a real-time Monte Carlo scatter calculation. Floyd et al. pioneered studies in this field as early as the mid-1980s, although the limitations on computational resources prevented the method from maturing for clinical use [18]. However, today it is possible to perform fast and accurate scatter modelling for individual patient geometries and source distributions [19]. In these methods, the activity distribution at various steps in an iterative reconstruction process are linked to an external Monte Carlo-based forward projector that, based on the estimated activity distribution, calculates a projection that fully includes the modelling of scatter in non-uniform regions. The method has been proven clinically useful mainly because of the implementation of fast variance reduction methods especially when modelling the collimator response, and studies have so far been made for ^{99m}Tc [20, 21] and ^{201}Tl [22]. This method also can include a compensation for septum penetration in the collimator and backscatter for components behind the crystal, and can therefore be useful for studies on ^{131}I as well [23].

18.3.4 Spatial Resolution Compensation Methods

Compensation for the degradation in spatial resolution due to the collimator-response function (CRF) improves spatial resolution and provides improved quantitative accuracy for small objects. There are two classes of methods: iterative and non-iterative. Non-iterative methods include restoration filters, such as Metz and Wiener filters [24]. These filters are generally applied in the frequency domain to filter image data with a spatially invariant filter that describes the inverse of the PSF function. They will, however, not be as effective at removing spatial variation effects as compared to iterative methods and they tend to have poor noise properties since the inverse filters generally act as a high-pass filter, thereby amplifying noise.

In an iterative reconstruction method, the spatial resolution can be partly compensated for by including a model for distance-dependent blurring in the projector steps (forward and backward). This means that instead of forwarding the data in straight lines along the columns when cal-

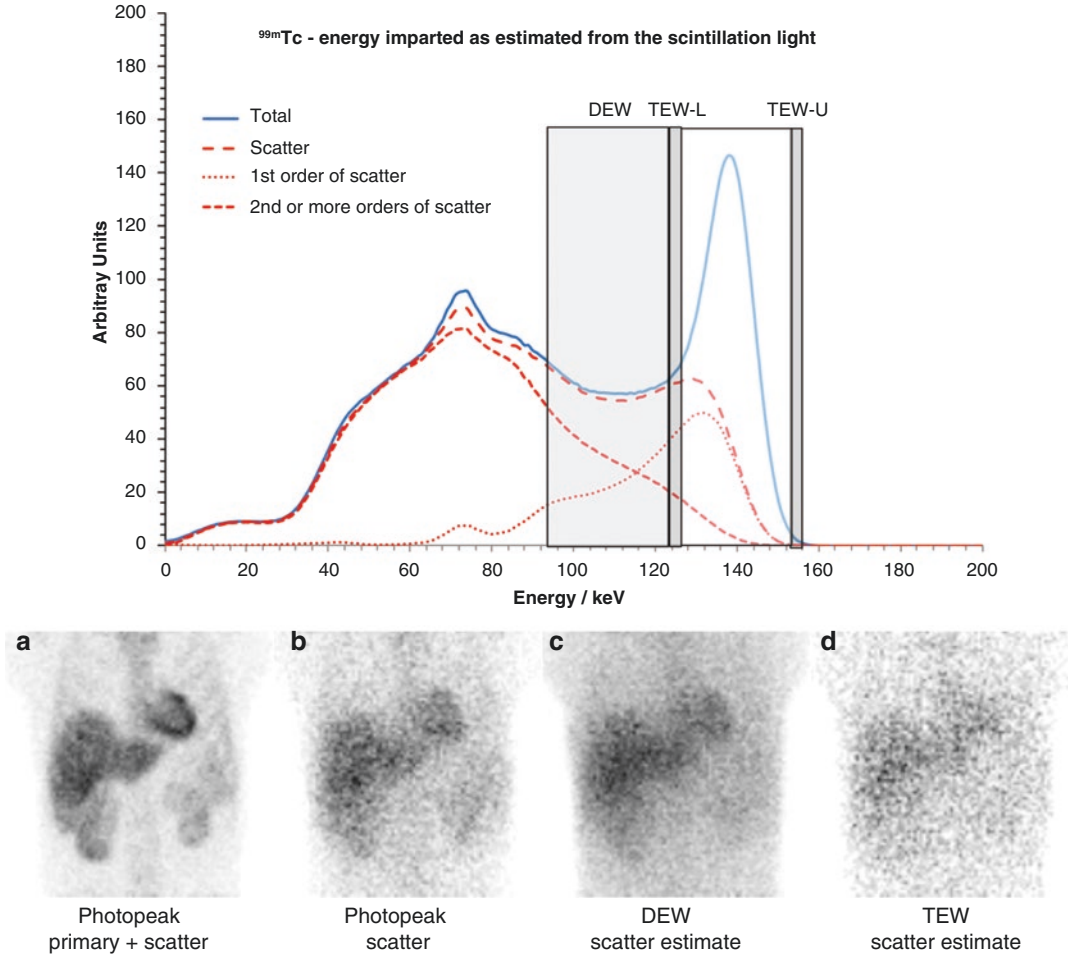

Fig. 18.9 Plot shows the location of the DEW and TEW windows. Image (**a**) shows an image with events from both primary and scattered photons. Image (**b**) shows the true scatter in the photon-peak energy window. Image (**c**) shows the estimation of scatter distribution by a lower wider energy window (DEW method). Image (**d**) show estimation of scatter by TEW method where two narrow energy windows (width 4 keV) is positioned on each side of the main photon-peak window. The simulated spectrum has been divided into total, scatter, first order scatter and second or more orders of scatter. It can be seen that there are two or more orders of scattered events in the DEW region as compared to the photo-peak region. This means that the distribution of scatter will be different in the DEW window, which will result in both over- and under-corrections when subtracting the data from the photo peak window. The difference in distributions can be seen in the images. The problem of noise in the TEW windows due to the narrow energy window size is also evident

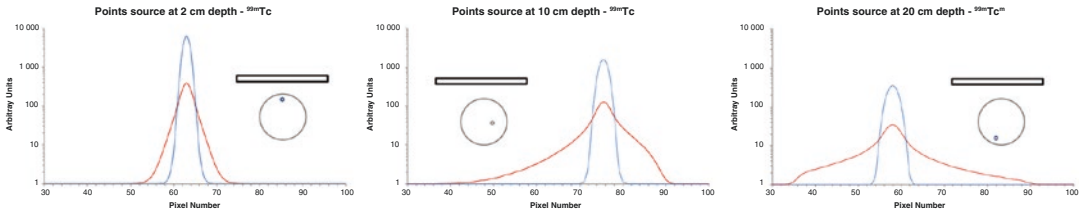

Fig. 18.10 Point-spread functions for three locations inside a cylindrical water phantom. The primary unscattered component is shown as dashed lines. Note the shade in the distribution of the scatter as a function of source depth. Please note the non-symmetry as well

culating the projection value, the projector includes the probability of a photon to pass nearby holes. This spread is often described by a distance-dependent, spatially invariant Gaussian function, but images of the point-spread function can also be explicitly calculated and stored for each distance by Monte Carlo simulation for those cases where septum penetration is important (i.e. imaging with ^{131}I and ^{123}I radiopharmaceuticals). The correction method has an effect similar to low-pass filtering, but it is not perfect in that sense that perfect resolution is not restored since some information about high spatial frequencies is permanently lost. Iterative reconstruction CRF compensation also produces different noise patterns compared to the filtered back projection methods or iterative reconstruction without CRF correction. The correction method tends to increase the noise in the mid-frequency range, which may result in a blobby pattern in the reconstructed images, but noise properties can be improved by the accurate modelling of CRF [25]. Some recent software programs have been written to reduce acquisition time by incorporating resolution recovery into the reconstruction process. This helps to improve the resolution properties of the image and hence, signal-to-noise ratios for data acquired with lower count statistics [26].

The degradation of spatial resolution is a function of the distance from the face of the collimator. Thus, a pre-requisite to model the CRF is the information regarding the distance from the COR to the collimator face for every acquisition angle along with the knowledge of the collimator characteristics. For systems that use circular orbits, this information is defined by the radius of rotation. For SPECT system, the distance between the camera and the patient corresponding to each angle can be fine-tuned by sensors on the scintillation camera head. If this method is used, then a CRF correction requires information regarding the variation of organ-to-collimator distances for a particular projection angle. This is the type of information that, however, is not always available from commercial systems or Dicom file headers.

18.3.5 Full Monte Carlo-Based Image Reconstruction

A full Monte Carlo simulation of the radiation transport using a mathematical description of the patient CT and toward the camera has the potential to model all the important physical events that will ultimately affect the formation of a SPECT projection. This means that, if such a model can be included in an iterative reconstruction method, the compensations for physical effects should be more accurate than methods based on approximations such as the DEW and TEW scatter corrections, neglecting scattering in the collimator and related X-ray emissions and backscattering from the surrounding camera housing. Furthermore, since there is a relation between emitted photons (activity) and registered counts for a given source/camera configuration, a reconstructed set of images based on a Monte Carlo model can provide voxel values in terms of the unit of activity (Bq) and thus removing, in principle, the need for separate calibration [27].

A full Monte Carlo simulation of the imaging system can be applied in the forward projection step of an iterative reconstruction procedure. An MC-based back projector step is, however, more difficult to implement and therefore, a dual-matrix OS-EM approach can be adopted using a more simplified model of the radiation transport in the back projection [28–30]. This can be justified since the back projection step more has an effect on the rate of convergence and noise properties [31, 32].

The main limitation of MC simulations is the large computational burden and, consequently, the need for fast computers. It is, therefore, not likely that MC-reconstruction will be a useful tool for routine reconstructions, especially since there might not be a need for it in many cases. However, if the calculation time is not crucial or a ‘second opinion’ is required, a full Monte Carlo-based image reconstruction may provide more comprehensive information regarding the radionuclide distribution. Full MC-based reconstruction may also be of importance in the imaging of radionuclides with complex decay schemes

such as for ^{131}I [33] and ^{166}Ho [30], or when imaging bremsstrahlung photon emission from β-particle emitting radionuclides such as ^{90}Y [29, 34, 35].

18.3.6 Partial Volume Correction

Reconstructed SPECT images obtained by FBP or iterative reconstruction are degraded by the limited spatial resolution of the collimator system resulting in significant partial volume effects [36]. Because of this effect, spill-in of counts can be significant when evaluating the activity in small regions located in close proximity to neighbouring objects with high activity uptake. In a similar manner, spill-out occurs when quantifying high activity and activity concentrations in small regions. In these cases, it might therefore be of importance to include some kind of partial volume correction (PVC) (Fig. 18.11).

Partial volume effects are of particular interest in clinical applications such as the determination of myocardial wall thickness, in quantitative brain studies where activity concentrations in small structures will be underestimated, and in dosimetry for radionuclide therapy where uptake by small tumours may be important for accurate dose assessment.

The underlying assumption for most PVC methods is that the radioactivity uptake in a specific volume is uniformly distributed, and that the change in counts in this volume can, therefore, be used to develop a correction method. A simple and practical method for partial volume compensation is the use of volume-dependent recovery coefficients which have been determined from either experimental measurements of spheres of various sizes in physical phantoms [37–39] or mathematical simulation. Recovery factor is defined as the ratio between the measured activity in a defined volume and the true activity in the same volume ($RC = A_{meas}/A_{true}$) and is determined for different activity volumes. If the ratio is unity, there is no issue with PV and the correct activity is estimated from the images. However, because of the spatial resolution, this will not be the case for small objects. Figure 18.12 shows an example of the dependence of RC curves on spatial resolution. In practice, the value RC_{vol} that matches the current activity volume and the correct the activity A obtained from the volume with the selected RC ($A' = A/RC_{vol}$) as closely as possible is selected from these RC curves.

The accuracy of RC correction methods is, however, highly dependent on the shape of the object and the background activity of the target structure.

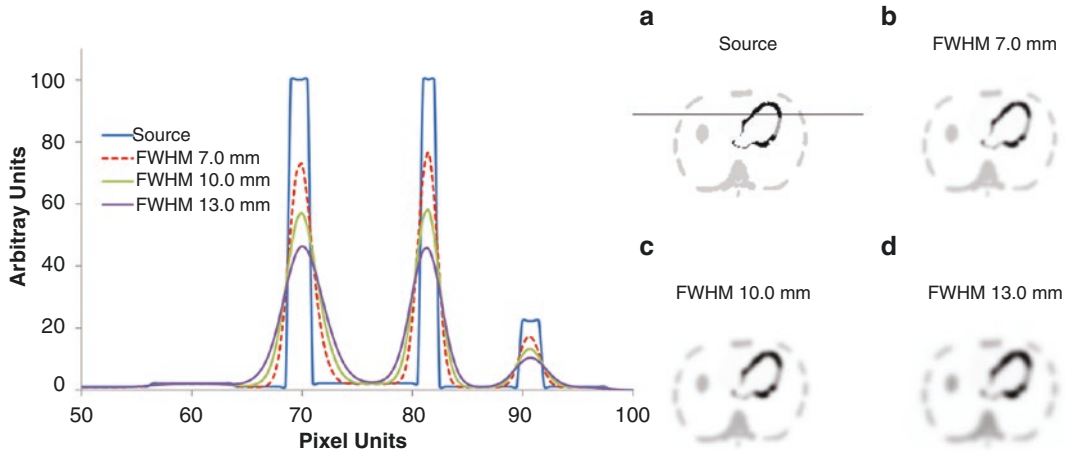

Fig. 18.11 Effect of partial volume. (**a**) shows the activity distribution ('source') and (**b**)–(**d**) shows the image blurred by a Gaussian function that simulates three different spatial resolutions. The profiles through the heart show the 'spill-in' into the left ventricle and 'spill-out' from the myocardial region

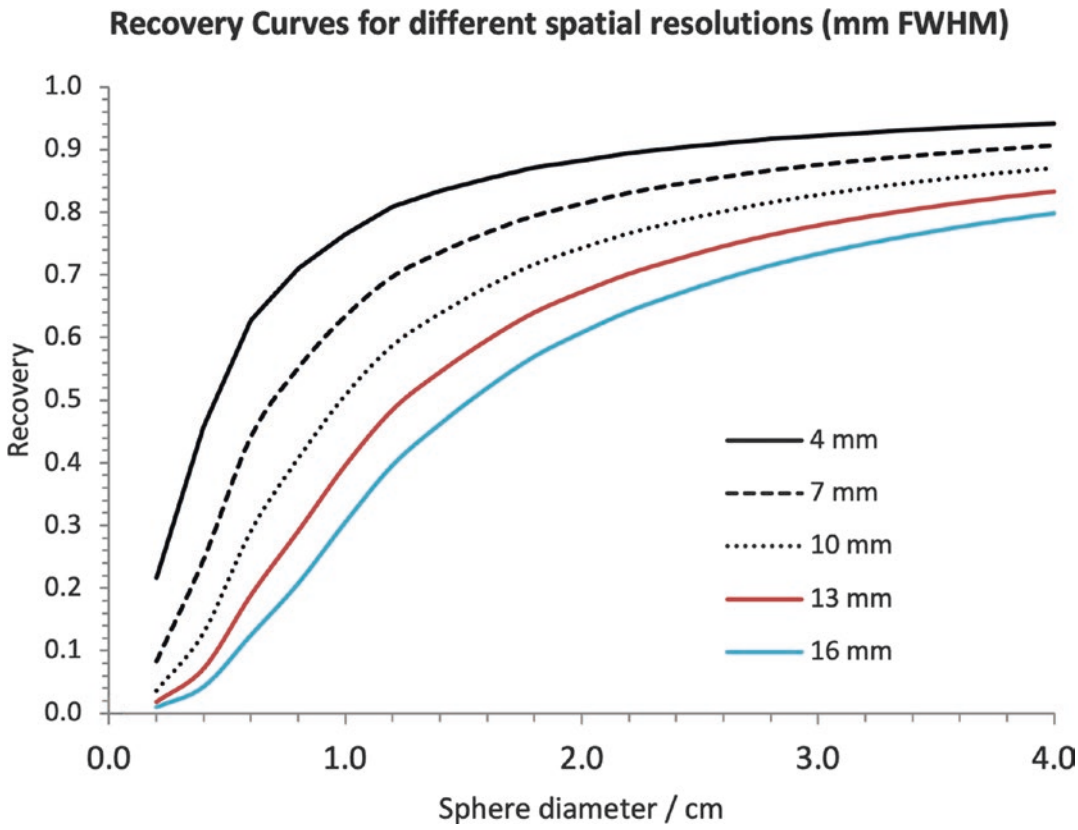

Fig. 18.12 Recovery curves obtained for five different simulated FWHM values of a hypothetic camera system. Initial spherical volumes were created as 3D-images, which were then convolved with a Gaussian function of different standard deviation values (recalculated from the FWHM values according to the relationship FWHM = 2.35 σ). The fraction of counts that appear outside the initial volume after the convolution were then calculated and from these, the displayed RC curves were obtained

A more general approach is to minimise the resolution and penetration effects by implementing a 3D depth-dependent detector response included into the system model of an iterative reconstruction. These implementations have resulted in improved quantification accuracy for higher energy photon emitters such as ^{111}In and ^{131}I [40–42]. However, these studies show that for small targets and targets within a high background activity, the activity recovery is not complete even when a 3D depth-dependent detector response function is included in the system model.

As dual modality SPECT-CT imaging with good image registration has become available recently, there is much incentive to use the CT based anatomical information to correct for partial volume effects. CT-defined templates have been used for SPECT partial volume correction in myocardial studies [43] in which user-defined templates were mathematically projected to mimic the SPECT process followed by image reconstruction to obtain a pixel-by-pixel PVC for the myocardial region. In more recent SPECT studies, the original template-based PVC was modified to implement a perturbation-based template method, which accounts for the non-linear effects of the iterative reconstruction [42, 44, 45]. Thus, it could be concluded that quantitative accuracy has been demonstrated for SPECT studies with ^{99m}Tc, ^{111}In and ^{131}I.

18.3.7 Conversion from Counts to Activity

Since a SPECT system measures the number of detected events from photons interacting in the NaI(Tl) crystal and determines a measure of the position for that interaction, an additional step is necessary to obtain an estimate of the activity in the source behind these events. The conversion from the count rate to activity is, therefore, a crucial part of the quantitative procedure. In most cases, a parallel-hole collimator is used in the investigation. In one sense, one can define such a collimator as a number of individual detectors that together determine the final detection of the counts. For a single hole, the probability for detection is determined by the hole-dimension and distance to the source. When considering a single collimator hole, the detection capability of photons passing though this hole depends of the inverse of the square of the distance, but because of the multiple holes, the possibility of a photon to pass through them increases with the square of the distance, resulting in that the total number of detected counts remains the same independent of the distance to the camera. This, however, holds true only for moderate distances from the camera and not very close to the collimator surface. Thus, the number of counts detected will depend on the (a) the collimator design, absorption efficiency of the crystal and (b) size and location of the energy window. The system sensitivity is defined by NEMA (The Association of Electrical Equipment and Medical Imaging Manufacturers) [46] and are measured in a standardised manner by the vendors. Therefore, one can obtain a single conversion factor from cps to MBq. However, the distribution of detected counts depends very much on the source-to-collimator distance so if one want to determine the activity in a ROI (2D) or a VOI (3D) there will be a need to consider the 'spill-out' and 'spill-in' of counts from the ROI/VOI due to the effect of the spatial resolution. The determination of the activity therefore will be dependent of the ROI/VOI that have been defined and therefore, in principle, require a recovery factor for each possible shape we define.

The main purpose of a reconstruction program is to redistribute counts measured along a projection bin back to the origin, from which the photons were emitted that resulted in the detected counts. This means that, for a carefully designed program, the total number of counts in a 3D reconstructed volume should be equal to the number of counts acquired by the camera and if good scatter and attenuation compensation are made, the activity should be possible to be determine from the system sensitivity. Again, this is not the same as saying that the activity in a VOI correct. The quantitation in a VOI can be described by the following eq. [47],

$$A_{\mathrm{VOI}} = \mathrm{cps}_{\mathrm{VOI}} \cdot \frac{1}{\mathrm{RC}_{\mathrm{obj}}} \cdot \frac{1}{\left(\mathrm{cps}/\mathrm{MBq}\right)_{\mathrm{FOV}}} \tag{18.10}$$

where the activity A_{VOI} in a VOI is determined by the product of (a) the count rate cps_{voi} measured in an VOI, (b) the RC_{obj} which is the recovery coefficient for an object that best match the dimension of the VOI and (c) the system sensitivity $(cps/MBq)_{FOV}$ as have been measured in a FOV of the camera. This assumes that the cps_{voi} has been obtained from an image, corrected for scatter and attenuation.

If it is not possible to correct for the entire expected degradation effect and thus apply the above equation, a common procedure is to calibrate the study against an experimental phantom measurement. A phantom and source are selected so that they mimic the patient's geometry and activity distribution as closely as possible and then a SPECT measurement is conducted using the same acquisition- and reconstruction parameters as for the patient measurement. By knowing the activity in the experimental source, one can determine a calibration factor (also in units of cps/MBq) that can be used to determine the activity in the patient-defined VOI. By doing this, it is assumed that the additional effects cancel out because of the calculation procedure. However, one should remember that the calibration factor is, in principle, only valid for the geometry from which it has been derived.

18.4 Influence of Correction Algorithms on Image Quality

Photon attenuation is the single largest factor that degrades the image quality in SPECT. Without proper compensation for attenuation, an absolute estimate of the activity will often be in error by >50%. The magnitude of the effect is higher for low-energy photons and for large parts of the body with high density. Non-uniform attenuation in the head or the thorax can cause undesirable artefacts that impede both visual interpretation and activity quantitation.

Energy window-based scatter correction methods can be applied in two ways; either (a) prior to reconstruction by subtracting the estimated scatter from the projection data prior to reconstruction or (b) incorporating the scatter estimate in an iterative reconstruction method. The disadvantage of the first approach is the fact that subtracting the two noise images results in increasing the noise. This means that some kind of low-pass filtering may need to be applied on the data, resulting in a degradation of the spatial resolution of the image. The second approach of incorporating the measured scatter estimate in the forward projection has shown to have better noise properties and is probably more widely accepted in commercial systems. Accurate scatter correction techniques should improve image contrast and lead to better quantitative accuracy.

The necessary for quantitative SPECT images depends on the application. It is, however, important to understand that even if the actual number in units of MBq or MBq/mL is not important for a particular application, quantification procedures may improve the accuracy and precision in the investigation since compensations correct for the misplacement of counts and thus, provide a better image. On the other hand, if the correction methods used are not properly set up and validated, this can lead to problems. Furthermore, in some cases, image noise can be amplified which is a degrading factor for the image quality despite the theoretical improvement due to a particular compensation.

It is now common to improve the image resolution SPECT by including collimator compensation in the tomographic reconstruction. This can be achieved by modelling the manner in which the photons also pass through the nearby collimator holes. One method to do this during the projector/back projector step is to separate the modelled projection as a function of distance. The different projections are then filtered by a function that describes the PSF for a particular distance (often a Gaussian function). The results of each individual filtering process are then added to a final projection. Addition effects, such as, star-artefacts as a result of septal penetration and collimator scatter can also be included. However, one should be aware of the creation of the edge artefacts as a result of these types of compensations. These artefacts appear as ring-shaped areas of too-low or too-high [36, 48] counts, often close to sharp boundaries (i.e. gradients of counts). This effect does not change the total number of counts in the image if the PSF filters are properly normalised, but it thereby creates a count distribution that does not reflect the actual activity uptake and this can hamper further analysis of, for example, heterogeneity within a volume-of-interest. Figure 18.13 shows an example of these effects.

Despite the many inherent problems with SPECT images the recent advancement in developing correction methods for physical effects, such as photon attenuation, scatter and collimator resolution has made SPECT a quantitative tool for activity measurement. Figure 18.14 shows an example of state of the art reconstruction and activity quantification method including non-uniform attenuation correction, scatter correction using the ESSE method [49] and spatial variant collimator-response correction.

18.5 Applications of SPECT in Dosimetry

One of the areas in nuclear medicine applications that rely on the absolute values of the SPECT images is dosimetry in radionuclide therapy where multiple SPECT acquisitions form the base for therapeutic dose planning. The quantity of the absorbed dose is used to relate the energy

Fig. 18.13 Figure shows the artefacts introduced by the collimator-response compensation. Left image (**a**) shows three spheres reconstructed with scatter and attenuation compensation. Right figure (**b**) shows the same reconstruction including where ´collimator-response compensation (Gaussian) has been included. The hole in the centre of the spheres can clearly be seen

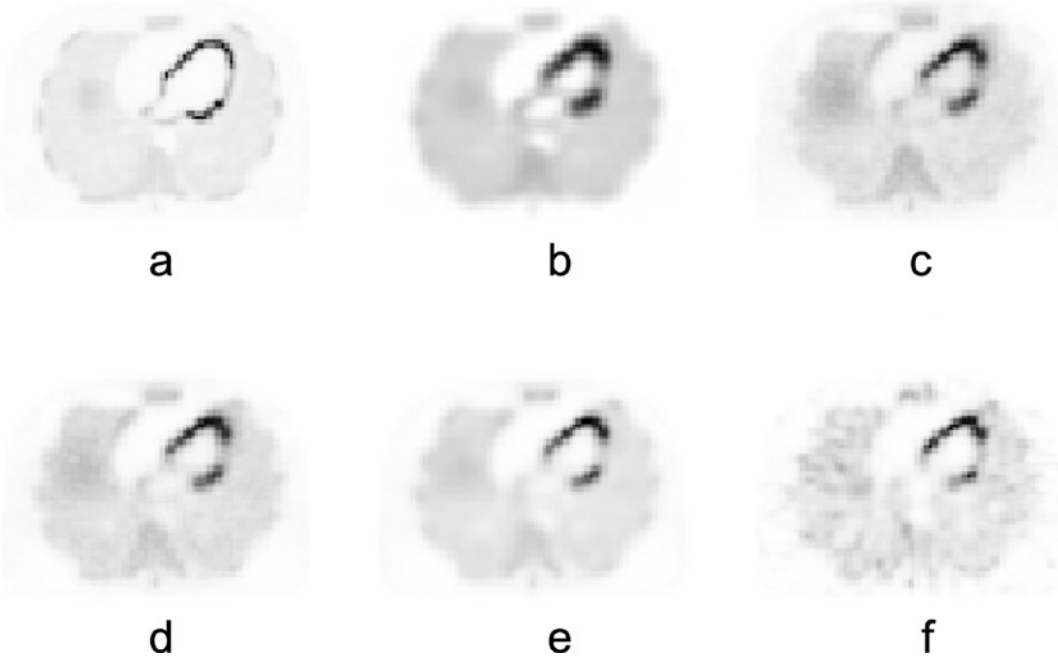

Fig. 18.14 Image (**a**) is reconstructed data mimicking a perfect system without patient movements (the image is equal to Fig. 18.7a). Image (**b**) shows an image of the same data set reconstructed with FBP without corrections. A Butterworth filter with cutoff 0.5 and order 2 was used. Figures (**c**–**e**) shows images reconstructed with OS-EM (six iterations and ten subsets) using non-homogeneous attenuation correction (**c**), attenuation and scatter correction using the ESSE method (**d**) and scatter and attenuation correction together with CRF correction (**e**). Image (**f**) shows an image reconstructed with all correction methods but using a data set with a realistic noise level added

imparted by ionising radiation to a biologic effects and is defined as the mean energy imparted, $\mathrm{d}\bar{\varepsilon}$, to the matter in an infinitesimal volume, dV, with mass dm [50, 51], according to

$$D = \frac{\mathrm{d}\bar{\varepsilon}}{\mathrm{d}m} \tag{18.11}$$

The SI-unit of the absorbed dose is Gy (1 J/kg) and its value can vary between different parts of an organ or tissue. For cases where there is local difference in the activity uptake and hence the energy delivery, the mean absorbed dose, can be calculated according to

$$D_{\mathrm{T}} = \frac{1}{m_{\mathrm{T}}} \int_{m_{\mathrm{T}}} D\,\mathrm{d}m \tag{18.12}$$

where m_{T} is the mass of a tissue or organ, or some other target volume for which the absorbed dose is determined [52].

18.5.1 The Basic Calculation Scheme

The basic equation for dose calculations has been given by an MIRD publication [53] and is described as

$$D = \frac{1}{m(r_{\mathrm{T}})} \sum_{r_{\mathrm{s}}} \left[\int_{T_1}^{T_2} A(r_{\mathrm{s}}, t)\,\mathrm{d}t \sum_i \Delta_i \cdot \phi(r_{\mathrm{T}} \leftarrow r_{\mathrm{S}}, E_i, t) \right] \tag{18.13}$$

where n is the number of particles i per disintegration, Δ_i is the average energy emitted for particle i, ϕ is is the absorbed fraction—a geometrical related factor that describe the fraction of energy emitted from a source volume element r_{S} that is absorbed in a target volume element r_{T}. Finally, m is the mass of the target volume element r_{T}. The time integral is the cumulative activity, $\tilde{A}$, and represent the total number of decays between a time interval T_1–T_2. Often this is calculated from the time of injection to infinity. The above equation can be understood as a product of two terms where on term $\tilde{A}$, is proportional to the total number of emitted particles emitted from the source during the time interval and the remaining terms, grouped into a term, called S, describe the radiation transport of energy from this source volume to the target volume, as described by the following

$$D = \sum_{r_{\mathrm{s}}} \tilde{A}(r_{\mathrm{s}}) \cdot S(r_{\mathrm{T}} \leftarrow r_{\mathrm{S}}) \tag{18.14}$$

where $\tilde{A}$ is a function of the chemical properties of the radiopharmaceutical and the biokinetic distribution while S is a function of the geometry and the physical properties of the radionuclide and the tissue composition. In some cases, $\tilde{A}$ and S represent a population and values can therefore be tabulated but in general both $\tilde{A}$ and S are patient-specific.

In practice, the activity integral $\tilde{A}$ (or the 'area-under-the-curve') is mostly determined by a curve-fitting procedure from a limited number of time-activity values as have been measured by a scintillation camera or SPECT. The cumulative activity then equals the area under the curve and if expressed per unit administered activity is called the residence time.

The estimation of risks for developing cancer due to the usage of radiation is calculated using pre-calculated S values that have been developed by Monte Carlo calculations for the generic mathematical description of a population of interest. This is because such risk estimations are only relevant to a large population of individuals. Therefore, such mathematical descriptions represent a reference male or female i.e. an average of a large population. These S value tables have been compiled in terms of the absorbed dose (Gy) to the target volume per cumulative activity (MBq h) in the source organ. S values are embedded into programs, such as, the OLINDA code [54]. However, the mathematical phantoms have not been developed for individual therapy planning and therefore the dose-conversion factors are not very well representative. To overcome this, one may need to implement the patient's own geometry and biokinetics into a dose calculation Scheme. A principal flowchart showing the steps necessary to consider for 3D patient-specific SPECT (and PET) dosimetry is shown in Fig. 18.15.

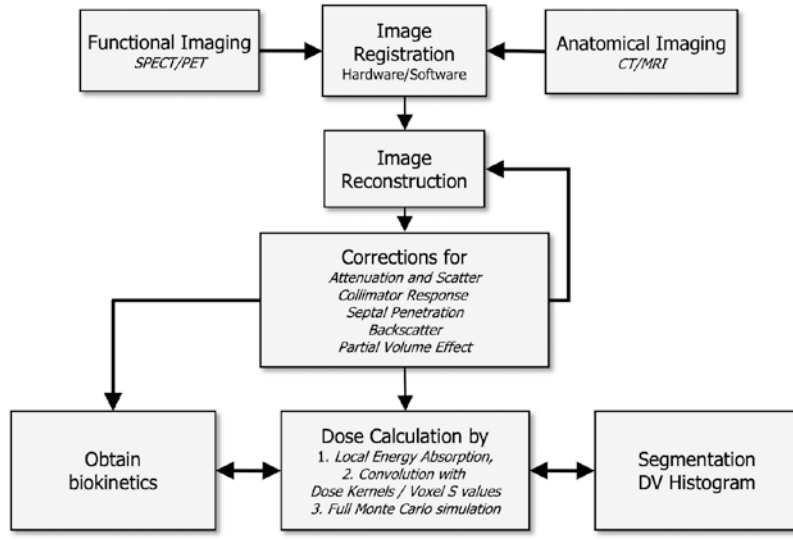

Fig. 18.15 Flowchart describing the different steps toward a dosimetry calculation based on quantitative SPECT images

18.5.2 Dose Calculation from Quantitative SPECT Imaging

Most dosimetry studies with scintillation cameras are conducted by planar scintillation camera imaging using the conjugate-view method. As described earlier, this method relies on opposite projections and if taking the geometrical-mean of the opposite projection, the dependence on the source depth is greatly reduced. The attenuation correction then depends only on the thickness of the patient (compared to attenuation correction in PET). The method, however, has several drawbacks. First, the above statement is only valid for a point source. If extended sources are being imaged, (which always is the case in clinical studies) then a correction for the source thickness needs to be made [55]. Second, if over and underlying activities are present then this affect the quantitation since the planar imaging is on a 2D modality and corrections needs to be made [56]. Third, scatter correction and septum penetration may not be accurately modelled and fourthly, the dosimetry needs in most cases to rely on *S*-factors obtained from a mathematical phantom.

SPECT in combination with CT can overcome many of these drawbacks because of the inherent 3D activity determination. The methods, described below, treat each voxel as a source volume and correspondingly, each voxel as a target organ. In practice, one does not store the *S*-factor that corresponds to each combination, but the MIRD equation will remain valid in these cases. The results will be 3D images of absorbed dose distributions useful to obtain, for example, dose-volume histograms and other parameters related to the heterogeneity of imparted energy within the volume of interest.

18.5.3 Energy Locally Absorbed Within a Voxel

In its simplest form, a dose calculation based on quantitative SPECT can assume all kinetic electron energies emitted from the radionuclide as locally absorbed within the voxel volume and disregard the energy distribution from the photons. The absorbed dose is then calculated from the mass of the volume element. This assumption is not as approximate as it sounds because the spatial resolution of a SPECT image used as input is in the same order or larger compared to relevant electron ranges. Thus, the SPECT image may very well show the absorbed dose distribution from electrons. If reviewing the general MIRD equation above, this method corresponds to the case where the target volume equals the source volume ($r_T = r_S$). This type of calculation

may work only on pure β-emitting radionuclides such as ^{90}Y or when the contribution to the absorbed dose from photons can be regarded as negligible.

18.5.4 Convolution Based on Point-Dose Kernels

This method uses a pre-calculated energy distribution in 3D from a point source usually stored as function of the radial distance from the point source normalised to the energy emitted per disintegration. By a mathematical convolution either in the spatial domain or frequency domain, the initial activity image (e.g. a SPECT image) can be converted to absorbed dose images. Berger has published point-dose kernels for both photons [57] and electrons and β particles [58]. Convolution of SPECT images with point-dose kernels should generally be used when the voxel size of the activity matrix is small compared to the path length of the particles. The dose kernels are also generally valid for a uniform material (often water or tissue-equivalent material) and the calculation procedure (often performed in the Fourier domain) is spatially invariant and does not take into account variations either in density or energy distribution due to organ or patient boundaries.

18.5.5 Convolution Based on Voxel *S* Values

Most point-dose kernels are published as the radial distribution of energy from a point-like source. When applying these kernels to a set of voxel-based images, one needs to interpolate these functions to match the different voxel locations—a procedure that sometimes can be very tricky to get right. A more practical approach is to create so-called voxel *S* values where the energy deposition per unit activity in a centre voxel is calculated for each neighbour voxel for a particular voxel grid. Then, only a discrete convolution procedure will be needed. A restriction is that the voxel *S* values must match the voxel size of the image *A*. The dosimetry at a voxel level has been discussed in MIRD 17 [59] and voxel *S* values have been published by Lanconelli et al. [60] for different voxel sizes. A potential ambiguity with the voxel *S* value approach is the question of whether the source distribution used to calculate the *S* values should be a point source in the middle of a central voxel or if the decay locations should be sampled uniformly within the voxel. The approach selected could result in differences in the result for radionuclides emitting charged particles with a small range. If using a point source, many of the charge-particles may not reach the boundary of the voxel.

18.5.6 Full Monte Carlo Simulated Radiation Transport

The most accurate absorbed dose calculation, but also the most complex and computationally demanding procedure, is a full radiation transport calculation using the Monte Carlo method [61]. The method in this context starts from quantitative accurate SPECT images and registered density images, usually obtained from a patient-specific CT. From this set of images, simulation of individual photon and electron interactions are performed in the 3D density volume by tracing the particles to the end by explicitly simulating all relevant interaction types. The location of a decay corresponds to the apparent voxel location in the Cartesian coordinate system and the number of simulated decays is proportional to the voxel values of the quantitative SPECT images. The imparted energy from each particle is then scored in a matching 3D absorbed energy matrix as the particles are traced through the volume. When all the particles are simulated, the absorbed energy in each voxel per voxel mass gives the absorbed dose. The main advantage of a full Monte Carlo simulation is that it considers the patient geometry and heterogeneities in density and tissue compositions can be included in the absorbed dose calculation.

There are several very competent programs in the public domain which are useful for Monte Carlo absorbed dose calculations. The EGS fam-

ily of programs [62] have been shown to be useful and the simulation of voxel data is relatively straight forward—although it requires some programming skills. In Medical Imaging applications, the GATE Monte Carlo program [63] has attracted much interest due to its flexibility, especially with complex geometries. This program is a layer of the Geant4 program from CERN[1] and can simulate charged particles up to very high energies.

18.5.7 Considerations Related to Absorbed Dose Calculations Based on SPECT/CT Data

The new hybrid systems offer considerable potential for accurate dosimetry both in 2D and 3D. Today, most SPECT/CT systems are based on diagnostic CT acquisition with a spatial resolution of an order of magnitude higher than the SPECT unit. In some systems, the CT unit can be used to obtain useful information also about the attenuation for the planar conjugate-view method by performing a full-length scan (so-called scout measurement). If the scaling between pixel units and density can be determined, then this transmission image will be the correction necessary for planar attenuation correction [64]. The high-quality image obtained from diagnostic CT units makes accurate SPECT quantification possible, and the known limitations with radionuclide-based transmission sources (downscatter, noise and limited spatial resolution) is eliminated by using CT.

Some issues need to be considered when doing absorbed dose calculations based on SPECT data. The most important is the fact that the SPECT images do not show the actual activity distribution. The images are affected by the particular system degradation in spatial resolution and the effect (discussed above in the partial volume section) is dependent on the source volume.

When calculating the absorbed dose, it is convenient to use CT images if proper scaling to density can be achieved. However, in most modern systems, the spatial resolution of the CT data can be of an order of magnitude better than the SPECT information. When using high-resolution CT as mass images in the voxel-by-voxel absorbed dose calculation, artefacts can be introduced where 'counts' spills out in regions of low densities. In addition, gas in the abdominal parts can result in very high absorbed doses because of the low CT voxel values in combination with blurring due to the limited spatial resolution in SPECT images. One way to overcome this problem is to reduce the spatial resolution of the CT images by convolution with a PSF that match the resolution of the SPECT system.

Most CT units are very fast with respect to image acquisition. This means that a CT image over the thorax may more reflect a particular time segment of the breathing cycle. A SPECT projection is generally acquired over a much longer time meaning that the image reflects a count distribution averaged over the whole respiration cycle. This can thus introduce artefacts during the correction for attenuation and absorbed dose calculations, especially close to the lung boundaries.

Even if SPECT/CT images are accurately registered to each other in a hybrid system, there is a need for image registration when performing multiple SPECT/CT studies in order to obtain voxel-based time-activity curves. Image registration using CT-CT images are preferable here compared to SPECT-SPECT registration as they are more similar. However, if a diagnostic CT is used then the absorbed dose caused by multiple X-ray exposures can be significant. The problem can be reduced if the CT unit can be run in a 'low-dose' mode. The signal-to-noise ratio and spatial resolution may be reduced here, but for attenuation corrections and absorbed dose calculations, this is probably not a serious problem.

[1]CERN = European Organization for Nuclear Research, Genève, Switzerland.

18.6 Conclusion

Quantitative SPECT has become a reality today mainly because of the considerable improvements effected in reconstruction algorithms where the corrections for image degradation due to photon attenuation, contribution of events such as the scattering of photons in the patient, collimator and camera housing, and septum penetration can be made in a consistent and natural manner in the forward projector step. The limitations that existed in earlier radionuclide-based transmission measurement methods are eliminated when using high-quality attenuation maps created by CT detectors, which are integrated into the SPECT gantry. Hybrid SPCT/CT systems also provide registered functional and anatomical images, thus reducing the need for software registration methods although registered software may be required when working with multiple SPECT/CT studies. Many scatter correction methods still rely on measurements in the secondary energy window but along with the improvement in computing power, real-time Monte Carlo simulation of scatter may be feasible for clinical use within a few years.

References

1. Shepp LA, Vardi Y. Maximum likelihood reconstruction for emission tomography. IEEE Trans Med Imaging. 1982;1(2):113–22. https://doi.org/10.1109/TMI.1982.4307558.
2. Lange K, Carson R. EM reconstruction algorithms for emission and transmission tomography. J Comput Assist Tomogr. 1984;8(2):306–16. https://www.ncbi.nlm.nih.gov/pubmed/6608535.
3. Hudson HM, Larkin RS. Accelerated image reconstruction using ordered subsets of projection data. IEEE Trans Nucl Sci. 1994;13:601–9.
4. Ljungberg M, Strand SE. A Monte Carlo program simulating scintillation camera imaging. Comp Meth Progr Biomed. 1989;29:257–72.
5. Ljungberg M. The SIMIND Monte Carlo program. In: Ljungberg M, Strand SE, King MA, editors. Monte Carlo calculation in nuclear medicine: applications in diagnostic imaging. Bristol and Philadelphia: IOP Publishing; 1998. p. 145–63.
6. Segars WP, Lalush DS, Tsui BMW. A realistic spline-based dynamic heart phantom. IEEE Trans Nucl Sci. 1999;46(3):503–6.
7. Segars WP. Development of a new dynamic NURBS-based cardiac-torso (NCAT) phantom. Ph.D., University of North Carolina, 2001.
8. Frey EC, Tsui BMW. A new method for modeling the spatially-variant, object-dependent scatter response function in SPECT. In Conference records of the IEEE medical imaging conference, Anaheim, CA, USA, 3–9 Nov 1996.
9. Berger MJ, Hubbell JR. XCOM: photon cross-sections on a personal computer. Washington, DC, . NBSIR 87-3597, -32676.: National Bureau of Standards; 1987.
10. Dewaraja YK, Ljungberg M, Koral KF. Characterization of scatter and penetration using Monte Carlo simulation in 131-I imaging. J Nucl Med. 2000;41(1):123–30. PM:0010647615.
11. Dewaraja YK, Ljungberg M, Koral KF. Accuracy of 131I tumor quantification in radioimmunotherapy using SPECT imaging with an ultra-high-energy collimator: Monte Carlo study. J Nucl Med. 2000;41(10):1760–7. PM:0011038009.
12. Slomka PJ, et al. "Motion-frozen" display and quantification of myocardial perfusion. J Nucl Med. 2004;45(7):1128–34. https://www.ncbi.nlm.nih.gov/pubmed/15235058.
13. Chang LT. A method for attenuation correction in radionuclide computed tomography. IEEE Trans Nucl Sci. 1978;25:638–43.
14. Jaszczak RJ, Greer KL, Floyd CE, Harris CC, Coleman RE. Improved SPECT quantification using compensation for scattered photons. J Nucl Med. 1984;25:893–900.
15. Ogawa K, Harata Y, Ichihara T, Kubo A, Hashimoto S. A practical method for position-dependent Compton-scatter correction in single photon emission CT. IEEE Trans Med Imaging. 1991;10(3):408–12. https://doi.org/10.1109/42.97591.
16. Frey EC, Tsui BMW. A new method for modeling the spatially-variant, object-dependent scatter response function in SPECT. In Conference records of the IEEE medical imaging conference, Anaheim, CA, pp 1082–1082, 1997.
17. Song X, Frey EC, Wang WT, Du Y, Tsui BMW. Validation and evaluation of model-based crosstalk compensation method in simultaneous 99mTc stress and 201Tl rest myocardial perfusion SPECT. IEEE Trans Nucl Sci. 2004;51 Part 1(1):72–9.
18. Floyd CE, Jaszczak RJ, Coleman M. Inverse Monte Carlo: a unified reconstruction algorithm for SPECT. IEEE Trans Nucl Sci. 1985;32:779–85.
19. Beekman FJ, de Jong HW, Slijpen ET. Efficient SPECT scatter calculation in non-uniform media using correlated Monte Carlo simulation. Phys Med Biol. 1999;44(8):N183–92. PM:10473218.
20. Xiao J, de Wit TC, Staelens SG, Beekman FJ. Evaluation of 3D Monte Carlo-based scatter correction for 99mTc cardiac perfusion SPECT. J Nucl Med. 2006;47(10):1662–9. https://www.ncbi.nlm.nih.gov/pubmed/17015903.

21. Liu S, King MA, Brill AB. Accelerated SPECT Monte Carlo simulation using multiple projection sampling and convolution-based forced detection. IEEE Trans Nucl Sci. 2008;55(1):560–8.
22. Xiao J, de Wit TC, Zbijewski W, Staelens SG, Beekman FJ. Evaluation of 3D Monte Carlo-based scatter correction for 201Tl cardiac perfusion SPECT. J Nucl Med. 2007;48(4):637–44. https://doi.org/10.2967/jnumed.106.037259.
23. Shaoying L, King MA, Brill AB, Stabin MG, Farncombe TH. Convolution-based forced detection Monte Carlo simulation incorporating septal penetration modeling. IEEE Trans Nucl Sci. 2008;55(3):967–74.
24. King MA, Schwinger RB, Doherty PW, Penney BC. Two-dimensional filtering of SPECT images using the Metz and Wiener filters. J Nucl Med. 1984;25:1234–40.
25. Beekman FJ, Slijpen ET, de Jong HW, Viergever MA. Estimation of the depth-dependent component of the point spread function of SPECT. Med Phys. 1999;26(11):2311–22. https://doi.org/10.1118/1.598745.
26. Borges-Neto S, et al. Clinical results of a novel wide beam reconstruction method for shortening scan time of Tc-99m cardiac SPECT perfusion studies. J Nucl Cardiol. 2007;14(4):555–65. https://doi.org/10.1016/j.nuclcard.2007.04.022.
27. Gustafsson J, Brolin G, Ljungberg M. Monte Carlo-based SPECT reconstruction within the SIMIND framework. Phys Med Biol. 2018;63(24):245012. https://doi.org/10.1088/1361-6560/aaf0f1.
28. Beekman FJ, de Jong HW, van Geloven S. Efficient fully 3-D iterative SPECT reconstruction with Monte Carlo-based scatter compensation. IEEE Trans Med Imaging. 2002;21(8):867–77. https://doi.org/10.1109/TMI.2002.803130.
29. Elschot M, Lam MG, van den Bosch MA, Viergever MA, de Jong HW. Quantitative Monte Carlo-based ^{90}Y SPECT reconstruction. J Nucl Med. 2013;54(9):1557–63. https://doi.org/10.2967/jnumed.112.119131.
30. Elschot M, et al. Quantitative Monte Carlo-based holmium-166 SPECT reconstruction. Med Phys. 2013;40(11):112502. https://doi.org/10.1118/1.4823788.
31. Zeng GL, Gullberg GT. Frequency domain implementation of the three-dimensional geometric point response correction in SPECT imaging. IEEE Trans Nucl Sci. 1992;39:1444–53.
32. Zeng GL, Gullberg GT. Unmatched projector/backprojector pairs in an iterative reconstruction algorithm. IEEE Trans Med Imaging. 2000;19(5):548–55. https://doi.org/10.1109/42.870265.
33. Dewaraja YK, Ljungberg M, Fessler JA. 3-D Monte Carlo-Based Scatter Compensation in Quantitative I-131 SPECT Reconstruction. IEEE Trans Nucl Sci. 2006;53(1):181. https://doi.org/10.1109/TNS.2005.862956.
34. Dewaraja YK, et al. Improved quantitative (90) Y bremsstrahlung SPECT/CT reconstruction with Monte Carlo scatter modeling. Med Phys. 2017;44(12):6364–76. https://doi.org/10.1002/mp.12597.
35. Lim H, Fessler JA, Wilderman SJ, Brooks AF, Dewaraja YK. Y-90 SPECT ML image reconstruction with a new model for tissue-dependent bremsstrahlung production using CT information: a proof-of-concept study. Phys Med Biol. 2018;63(11):115001. https://doi.org/10.1088/1361-6560/aac1ad.
36. Erlandsson K, Buvat I, Pretorius PH, Thomas BA, Hutton BF. A review of partial volume correction techniques for emission tomography and their applications in neurology, cardiology and oncology. Phys Med Biol. 2012;57(21):R119–59. https://doi.org/10.1088/0031-9155/57/21/R119.
37. Zito F, Gilardi MC, Magnani P, Fazio F. Single-photon emission tomographic quantification in spherical objects: effects of object size and background. Eur J Nucl Med. 1996;23(3):263–71. https://doi.org/10.1007/BF00837624.
38. Koral KF, Dewaraja Y. I-131 SPECT activity recovery coefficients with implicit or triple-energy-window scatter correction. Nucl Instrum Methods Phys Res, Sect A. 1999;422(1–3):688–92.
39. Geworski L, Knoop BO, de Cabrejas ML, Knapp WH, Munz DL. Recovery correction for quantitation in emission tomography: a feasibility study. Eur J Nucl Med. 2000;27(2):161–9. https://doi.org/10.1007/s002590050022.
40. Dewaraja YK, Wilderman SJ, Ljungberg M, Koral KF, Zasadny K, Kaminiski MS. Accurate dosimetry in 131I radionuclide therapy using patient-specific, 3-dimensional methods for SPECT reconstruction and absorbed dose calculation. J Nucl Med. 2005;46(5):840–9. http://jnm.snmjournals.org/cgi/content/abstract/46/5/840.
41. Ljungberg M, Sjogreen K, Liu X, Frey E, Dewaraja Y, Strand SE. A 3-dimensional absorbed dose calculation method based on quantitative SPECT for radionuclide therapy: evaluation for 131-I using Monte Carlo simulation. J Nucl Med. 2002;43(8):1101–9. PM:12163637.
42. He B, Du Y, Song X, Segars WP, Frey EC. A Monte Carlo and physical phantom evaluation of quantitative In-111 SPECT. Phys Med Biol. 2005;50(17):4169–85. https://doi.org/10.1088/0031-9155/50/17/018.
43. Da Silva AJ, Tang HR, Wong KH, Wu MC, Dae MW, Hasegawa BH. Absolute quantification of regional myocardial uptake of 99mTc-sestamibi with SPECT: experimental validation in a porcine model. J Nucl Med. 2001;42(5):772–9. https://www.ncbi.nlm.nih.gov/pubmed/11337575.
44. Yong D, Tsui BMW, Frey EC. Partial volume effect compensation for quantitative brain SPECT imaging. IEEE Trans Med Imaging. 2005;24(8):969–76.

45. Boening G, Pretorius PH, King MA. Study of relative quantification of Tc-99 m with partial volume effect and spillover correction for SPECT oncology imaging. IEEE Trans Nucl Sci. 2006;53(3 Part 2):1205–12.
46. Performance measurements of gamma cameras. In NEMA NU 1-2012, Virginia, 2013.
47. Ljungberg M, et al. MIRD pamphlet no. 26: joint EANM/MIRD guidelines for quantitative 177Lu SPECT applied for dosimetry of radiopharmaceutical therapy. J Nucl Med. 2016;57(1):151–62. https://doi.org/10.2967/jnumed.115.159012.
48. Rahmim A, Qi J, Sossi V. Resolution modeling in PET imaging: theory, practice, benefits, and pitfalls. Med Phys. 2013;40(6):064301. https://doi.org/10.1118/1.4800806.
49. Frey EC, Tsui BMW. Modeling the scatter response function in inhomogeneous scattering media. In Conference records of the IEEE medical imaging conference, 1993, pp 1–1.
50. U. International Commission on Radiation and Measurements. Report 85: fundamental quantities and units for ionizing radiation. J ICRU. 2011;11(1):1–31. https://doi.org/10.1093/jicru/ndr011.
51. Attix FH. Introduction to radiological physics and radiation dosimetry. Hoboken, NJ: John Wiley & Sons, Inc.; 1986.
52. U. International Commission on Radiation and Measurements. Report 86: quantification and reporting of low-dose and other heterogeneous exposures. J ICRU. 2011;11(2):1–77. https://doi.org/10.1093/jicru/ndr028.
53. Loevinger R, Berman M. A revised schema for calculation of the absorbed dose from biologically distributed radionuclides. MIRD Phamplet no. 1, revised. New York: Society of Nuclear Medicine; 1976.
54. Stabin MG, Sparks RB, Crowe E. OLINDA/EXM: the second-generation personal computer software for internal dose assessment in nuclear medicine. J Nucl Med. 2005;46(6):1023–7. https://www.ncbi.nlm.nih.gov/pubmed/15937315.
55. Fleming JS. A technique for the absolute measurement of activity using a gamma camera and computer. Phys Med Biol. 1979;24(1):178–80.
56. Sjogreen K, Ljungberg M, Strand SE. An activity quantification method based on registration of CT and whole-body scintillation camera images, with application to 131I. J Nucl Med. 2002;43(7):972–82. https://www.ncbi.nlm.nih.gov/pubmed/12097471.
57. Berger MJ. Energy deposition in water by photons from point isotropic sources: MIRD pamphlet no. 2. J Nucl Med. 1968;9:15–25.
58. Berger MJ. Distribution of absorbed dose around point sources of electrons and beta particles in water and other media: MIRD pamphlet no. 7. J Nucl Med. 1971;12:5–23.
59. Bolch WE, et al. MIRD pamphlet No. 17: the dosimetry of nonuniform activity distributions—radionuclide S values at the voxel level. Medical Internal Radiation Dose Committee. J Nucl Med. 1999;40(1):11S–36S. https://www.ncbi.nlm.nih.gov/pubmed/9935083.
60. Lanconelli N, et al. A free database of radionuclide voxel S values for the dosimetry of nonuniform activity distributions. Phys Med Biol. 2012;57(2):517–33. https://doi.org/10.1088/0031-9155/57/2/517.
61. Andreo P. Monte Carlo techniques in medical radiation physics. Phys Med Biol. 1991;36(7):861–920. https://doi.org/10.1088/0031-9155/36/7/001.
62. Nelson RF, Hirayama H, Rogers DWO. The EGS4 code system. Stanford, CA: SLAC, SLAC-265; 1985.
63. Jan S, et al. GATE: a simulation toolkit for PET and SPECT. Phys Med Biol. 2004;49(19):4543–61. https://doi.org/10.1088/0031-9155/49/19/007.
64. Minarik D, Sjogreen K, Ljungberg M. A new method to obtain transmission images for planar whole-body activity quantification. Cancer Biother Radiopharm. 2005;20(1):72–6. https://doi.org/10.1089/cbr.2005.20.72.